Influence of the Coriolis force on the velocity structure of gravity currents in straight submarine channel systems

R. Cossu,[1] M. G. Wells,[2] and A. K. Wåhlin[3]

Received 26 February 2010; revised 30 June 2010; accepted 7 July 2010; published 19 November 2010.

[1] Large-scale turbidity currents in submarine channels often show a significant asymmetry in the heights of their levee banks. In the Northern Hemisphere, there are many observations of the right-hand channel levee being noticeably higher than the left-hand levee, a phenomenon that is usually attributed to the effect of Coriolis forces upon turbidity currents. This article presents results from an analog model that documents the influence of Coriolis forces on the dynamics of gravity currents flowing in straight submarine channels. The observations of the transverse velocity structure, downstream velocity, and interface slope show good agreement with a theory that incorporates Ekman boundary layer dynamics. Coriolis forces will be important for most large-scale turbidity currents and need to be explicitly modeled when the Rossby number of these flows (defined as $Ro = |U/Wf|$, where U is the mean downstream velocity, W is the channel width, and f is the Coriolis parameter defined as $f = 2\Omega \sin(\theta)$, with Ω being the Earth's rotation rate and θ being the latitude) is less than order 1. When $Ro \ll 1$, the flow is substantially slower than a nonrotating flow with the same density contrast. The secondary flow field consists of frictionally induced Ekman transports across the channel in the benthic and interfacial boundary layers and a return flow in the interior. The cross-channel velocities are of the order of 10% of the along-channel velocities. The sediment transport associated with such transverse flow patterns should influence the evolution of submarine channel levee systems.

Citation: Cossu, R., M. G. Wells, and A. K. Wåhlin (2010), Influence of the Coriolis force on the velocity structure of gravity currents in straight submarine channel systems, *J. Geophys. Res.*, *115*, C11016, doi:10.1029/2010JC006208.

1. Introduction

[2] Submarine channels are the most significant morphologic features of the submarine landscape on the continental slope and are known to be the main conduits for turbidity currents to transport sediments to the deep ocean basins [*Meiburg and Kneller*, 2010]. There are still very few direct observations of turbidity currents moving through submarine channels [*Hay*, 1987; *Khripounoff et al.*, 2003; *Xu et al.*, 2004] since their infrequent occurrence, the great water depths and high current velocities make measurements difficult to obtain. Owing to the spatial extent of submarine channel systems and the associated long travel time, the flow properties and environments of those currents are likely to be deflected by Coriolis forces that arise owing to the Earth's rotation [*Menard*, 1955; *Komar*, 1969; *Wells*, 2009] for midlatitude and high-latitude systems. While the influence of Coriolis forces upon turbidity currents is acknowledged in several reviews [*Middleton*, 1993; *Huppert*, 1998; *Imran et al.*, 1999; *Kneller and Buckee*, 2000] and theoretical studies [*Komar*, 1969; *Bowen et al.*, 1984; *Nof*, 1996; *Emms*, 1999; *Ungarish and Huppert*, 1999; *Kampf and Fohrmann*, 2000], there have been very few previous experimental studies specifically focusing on turbidity currents on a rotating platform [*Wells*, 2009].

[3] One of the most noted effects of the Coriolis force upon well-developed levee systems is that the deflection of the turbidity current by Coriolis forces leads to an asymmetry between levee bank heights [*Menard*, 1955]. The right-hand-side channel levee (looking downstream) is consistently higher in the Northern Hemisphere [*Chough and Hesse*, 1976; *Klaucke et al.*, 1997, 1998; *Wood and Mize-Spansky*, 2009] and the left-hand-side channel levee is higher in the Southern Hemisphere [*Droz and Mougenot*, 1987; *Carter and Carter*, 1988; *Bruhn and Walker*, 1997]. These differences in levee height can be large, for instance in the North Atlantic Mid Ocean Channel (NAMOC hereafter), there is a difference in levee height that can reach more than 100 m and has an average difference of 65 m along a 950 km long section [*Klaucke et al.*, 1997]. Such observations of levee asymmetry are usually described in

[1]Department of Geology, University of Toronto, Toronto, Ontario, Canada.
[2]Department of Physical and Environmental Sciences, University of Toronto, Toronto, Ontario, Canada.
[3]Department of Earth Sciences, University of Gothenburg, Gothenburg, Sweden.

0148-0227/10/2010JC006208

the context of the theory of *Komar* [1969], although this theory has never been tested in laboratory-scale experiments on a rotating platform. In this paper the first rigorous test of this theory is presented as well as a complementary theory that quantifies the downstream and cross-stream velocity components.

[4] The basic description of rotationally influenced turbidity currents that is most widely used was presented by *Komar* [1969]. This theory is based on a simple momentum balance across the channel, whereby the pressure gradient forces that result from the surface slope of the turbidity current are balanced by the Coriolis and centrifugal forces. Turbidity currents are often constrained to flow in channelized systems, and it is usually assumed that the maximum levee heights are a good indication of the maximum thickness of the turbidity currents that formed the levee systems. If the difference in levee heights is a good measure of the maximum slope of the interface of the turbidity current, then the theory of *Komar* [1969] can be used to infer the magnitude of the mean current speeds of the typical turbidity currents that would have originally formed the channel levee system. There are several important simplifications made in the theory of *Komar* [1969] to describe the influence of Coriolis forces upon turbidity currents. First, it is assumed that the Froude number $Fr = U/\sqrt{g'h}$ (where U is the mean downstream velocity, g' the reduced gravity and h the thickness of the current), remains constant at a value of one. The use of a constant Froude number implicitly assumes that the rotation rate has no control on the velocity of the current, counter to the observations of *Cenedese et al.* [2004] and *Cenedese and Adduce* [2008], where laboratory experiments clearly show a large reduction in velocity when the Coriolis parameter is high. Another significant assumption in the theory of *Komar* [1969] is the neglect of boundary friction, which means that the Ekman boundary layers are ignored even though the Coriolis forces are assumed to be high. In a series of theoretical and experimental papers by *Wåhlin* [2002, 2004], *Davies et al.* [2006], and *Darelius* [2008], these boundary layers were shown to play a critical role in determining the sense of the secondary circulation in rotationally controlled gravity currents. Even in cases where Coriolis forces are not dominant, frictional effects have been shown to be important in determining the slope of a density interface flowing in a channel in estuaries [*Ott et al.*, 2002; *Chant and Wilson*, 1997; *Fugate et al.*, 2007; *Nidzieko et al.*, 2009].

[5] In contrast to the rarely observed turbidity currents, there are many direct observations of large-scale oceanographic density currents [*Ivanov et al.*, 2004] that can inform our understanding of the circulation patterns in turbidity currents. In the oceanographic literature there are a number of previous experimental studies on how Coriolis forces deflect cold or salty currents of dense water as they flow down the continental margins of oceans [*Griffiths*, 1986; *Price and Baringer*, 1994; *Etling et al.*, 2000; *Hallworth et al.*, 2001; *Cenedese et al.*, 2004; *Davies et al.*, 2006; *Cenedese and Adduce*, 2008]. These experimental studies found that rotating gravity currents rapidly come into a geostrophic balance, where the trajectory of the density current is determined by a balance between buoyancy forces, friction and Coriolis forces. Both density currents and turbidity currents are examples of gravity currents, in that the flows are primarily driven by density differences [*Huppert*, 1998]. Low concentration and weakly depositional turbidity currents exhibit concentration and velocity profiles that are very similar to saline currents [*Kneller and Buckee*, 2000]. For this reason many laboratory measurements using saline currents [e.g., *Keevil et al.*, 2006; *Islam et al.*, 2008; *Darelius*, 2008] have made important contributions to defining both the structure of the flow field and the turbulence intensities associated with these gravity currents and therefore helped to develop a general understanding of the fluid dynamics of turbidity currents. In this context we use experimental density currents for this study to understand the first-order effects of how Coriolis forces influence the circulation of channelized gravity currents, which will be also relevant to geologists wishing to comprehend the interaction of turbidity currents and channels they build. Nonetheless we note that further experimental work considering how sediment dynamics influence transport in Ekman boundary layers, will be needed to gain more insight into evolution of submarine channel systems subjected to Coriolis forces.

[6] Many submarine fan channels are confined by prominent levees, which form by deposition of suspended sediment on the slower moving margins of a turbidity current. These levees can grow rapidly, for instance, the average sedimentation rates during the active growth phases of the levees of the Amazon channel during the Pleistocene were 1 to 2.5 cm yr^{-1} [*Shipboard Scientific Party*, 1995]. The rapid growth has been attributed to deposition of suspended load as successive turbidity currents transit the channel and spill over the channel margins along their entire length [*Hiscott et al.*, 1997; *Peakall et al.*, 2000; *Straub et al.*, 2008]. In addition, recent nonrotating experiments on channelized turbidity currents have shown that the morphological evolution and associated depositional histories of submarine channel systems are highly influenced by the secondary flow structures within the channel, which determine where erosion and deposition will occur [*Corney et al.*, 2006; *Keevil et al.*, 2006; *Straub et al.*, 2008; *Islam et al.*, 2008; *Islam and Imran*, 2008]. The main focus in these nonrotating experiments has been to investigate the secondary circulation due to an imbalance of centrifugal and pressure gradient forces in channel bends, which plays a major role in the formation of superelevation of levee systems at the outer bend [e.g., *Straub et al.*, 2008]. Coriolis forces can also give rise to secondary flows within turbidity currents through the generation of Ekman boundary layers at the upper interface and the base of the flow. In the Northern Hemisphere these boundary layer flows will be directed to the left when looking downstream. To conserve volume there is return flow directed to the right in the interior of the flow. The basic features of such Ekman boundary layers in channelized currents have been seen in several laboratory experiments [*Benton and Boyer*, 1966; *Hart*, 1971; *Johnson and Ohlsen*, 1994; *Davies et al.*, 2006; *Darelius*, 2008; *Wåhlin et al.*, 2008]. Qualitatively similar secondary flows driven by Ekman boundary layer dynamics have been seen in oceanic gravity currents, such as reported in the Vema channel [*Johnson et al.*, 1976], in the Faroe Bank Channel [*Johnson and Sanford*, 1992; *Fer et al.*, 2010], in the Ellet Gully [*Sherwin*, 2010], and in the Baltic Sea [*Umlauf and Arneborg*, 2009a, 2009b]. Turbidity currents should also experience similar secondary flow patterns, when the flows

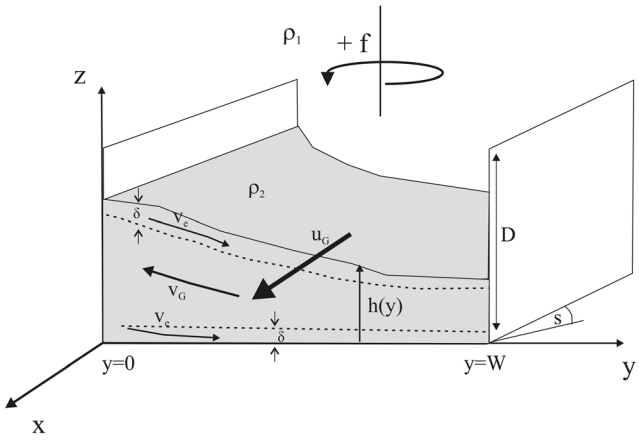

Figure 1. Schematic sketch of a density current flowing down a submarine channel with the gradient s, the channel height D, and the channel width W, looking upstream. The densities of the ambient fluid and the gravity current are ρ_1 and ρ_2, respectively, with $\rho_2 > \rho_1$. The main downstream flow is u_G, while there is also a significant transverse motion consisting of the interior flow v_G and bottom and interfacial currents v_e. The thickness of the Ekman boundary, δ, is small in comparison to the entire thickness of the flow, $h(y)$.

are at large enough scales that the Coriolis force becomes important.

[7] Though the theory of *Komar* [1969] has been cited almost one hundred times in the geological literature [i.e., *Bowen et al.*, 1984; *Klaucke et al.*, 1997; *Imran et al.*, 1999], no experiment has ever tested its validity. This is the first study to look at the flow structure in experimental rotating gravity currents and to relate it to a general geological context. Of primary importance for geologic applications is to infer the speed of the turbidity current that would have formed the asymmetric levees in a submarine channel, as this information can be used to determine the likely evolution of sediment deposition in turbidite beds that may be rich in hydrocarbons [*Weimer et al.*, 2000]. Using an analog experiment mounted on a rotating platform we are able to determine the dependence of the secondary flow structure, downstream velocity and interface tilt upon rotation rate. These observations are compared with the theory initially developed by *Wåhlin* [2002, 2004]. The paper starts with a discussion of the theoretical approaches to describe rotationally controlled gravity currents in channels by *Komar* [1969] and *Wåhlin* [2002, 2004] in section 2. The method and results are then described in sections 3 and 4, respectively. In section 5 the relationship between levee height and turbidity currents velocity is discussed in the context of some geological observations and we finish with our conclusions in section 6.

2. Theory

[8] The most widely used description of how Coriolis forces influence the dynamics of turbidity currents was proposed by *Komar* [1969], in which a force balance between the Coriolis force, the centrifugal force induced by flow curvature, and the pressure gradient force is assumed. Assuming that the upper interface has a constant slope and that friction is negligible, the momentum balance across the channel can then be written as

$$-g' \frac{dh}{dy} = fU + \frac{U^2}{R}, \tag{1}$$

where U is the mean downstream velocity, R is the radius of curvature of the channel, and f is the Coriolis parameter (defined as $f = 2\Omega \sin(\theta)$, with Ω being the Earth's rotation rate and θ the latitude). The reduced gravity is $g' = g(\rho_2 - \rho_1)/\rho_1$, where the gravity current has the density ρ_2 and ρ_1 is the ambient density of the seawater. Equation (1) can be rewritten in terms of a Froude number ($Fr = U/\sqrt{g'h}$) as

$$-\frac{dh}{dy} = Fr^2 \left(\frac{fh}{U} + \frac{h}{R} \right). \tag{2}$$

This momentum budget does not include any turbulence drag from the boundary and so implicitly assumes that stratification suppresses turbulent motions [e.g., *Chant and Wilson*, 1997]. On the basis of the force balance shown in equation (2) and assuming that $Fr = 1$, *Bowen et al.* [1984] expressed the difference in levee height due to the Coriolis effect in a straight channel as

$$\Delta h = Whf/U, \tag{3}$$

where $\Delta h = W\, dh/dy$, with W being the channel width and h being the depth of the main body of the flow. Equation (3) can also be written as $\Delta h/h = 1/Ro$ where $Ro = |U/Wf|$. Equation (3) is valid only for the straight sections of channels, where centrifugal effects are absent. Equation (3) has been used to describe observed channel height asymmetries, such as in the Amazon channel [*Imran et al.*, 1999], the Navy fan in California [*Bowen et al.*, 1984], or the NAMOC described by *Klaucke et al.* [1997, 1998].

[9] In a rotating system, the inclusion of friction into the momentum equation means that the Ekman boundary layers must be properly described. The resulting flow structure of a gravity current in a rotating system has been studied previously in the oceanographic literature [*Wåhlin*, 2002] and is illustrated in Figure 1. In the Northern Hemisphere the currents are deflected to the right side of the channel (looking downstream) until the flow reaches a geostrophic balance. Friction at the upper and lower boundaries leads to the formation of Ekman boundary layers, which drive a transverse, secondary circulation within the flow [see, e.g., *Darelius*, 2008]. Figure 1 shows a sketch of the flow structure. The secondary circulation consists of an across-channel flow in the Ekman boundary layers next to the bottom and next to the interface, and an oppositely directed across-channel flow in the interior away from the Ekman boundary layers. The thickness of the Ekman layers is δ, and the velocity there is v_e. In the interior the across-channel velocity is v_G. Similar secondary flows have been described in previous rotating laboratory experiments by *Hart* [1971], *Johnson and Ohlsen* [1994], *Davies et al.* [2006], *Wåhlin et al.* [2008], and *Darelius* [2008] and were also reported in oceanic gravity currents [e.g., *Johnson and Sanford*, 1992; *Sherwin*, 2010; *Fer et al.*, 2010]. In the work of *Umlauf and Arneborg* [2009a, 2009b] a different secondary flow struc-

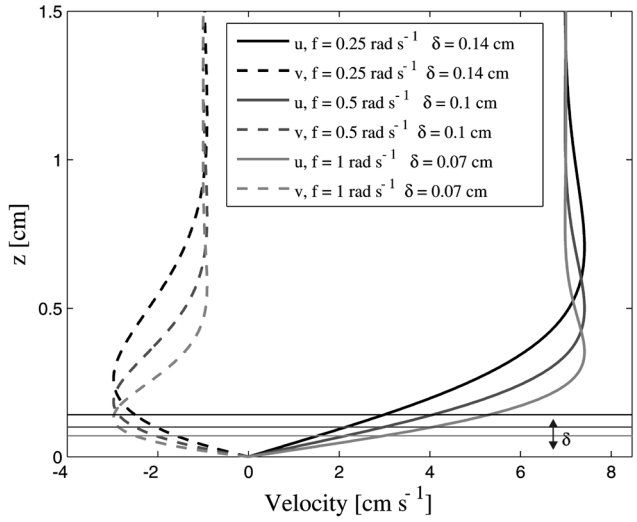

Figure 2. Dependence of the flow velocity u and v_e in the Ekman boundary layer on the Coriolis parameter f. Note also that the thickness of the Ekman boundary layer, δ, varies with f and is indicated by the horizontal lines.

ture was observed, with a thin jet in the interfacial layer and no clear Ekman layer in the bottom. This may be due to the fact that the Ekman layer was comparable in thickness to the flow itself.

[10] The Ekman boundary layer dynamics of a gravity current were previously examined for V-shaped [see, e.g., *Davies et al.*, 2006; *Darelius and Wåhlin*, 2007; *Darelius*, 2008], cosine-shaped [*Wåhlin*, 2002; *Darelius and Wåhlin*, 2007], and parabolic-shaped [*Darelius and Wåhlin*, 2007] canyons and ridges. In this paper a square channel is investigated for the first time, which permits analytical expressions for the across- and along-channel components of the velocity and the transverse slope of the interface, as a function of the rotation rate and mean slope of the channel.

[11] Consider a rectangular channel of width W, which slopes downward at angle s to the horizontal (Figure 1). Assuming a force balance between Coriolis, bottom friction, and pressure gradient, and a 1.5 layer system, the momentum equations can be written as

$$-fv = -g's - \nu\frac{\partial^2 u}{\partial z^2}, \tag{4}$$

$$fu = -g'\frac{dh}{dy} - \nu\frac{\partial^2 v}{\partial z^2}, \tag{5}$$

where f is the Coriolis parameter, v is the velocity in the across-channel (i.e., y) direction, g' is the reduced gravity, ν is the molecular viscosity, u is the velocity along the channel, and $h(y)$ is the thickness of the dense layer. Note that equation (5) in similarity with equation (1) expresses the interface slope as a function of the along-channel velocity. The difference is that equation (5) includes the viscous term (last term on right-hand side) but does not include the centrifugal term which is absent in straight sections. Away from the Ekman boundary layers, the viscous terms can be neglected and equations (4) and (5) reduce to the geostrophic velocities; that is,

$$v \to v_G = \frac{g's}{f}, \tag{6}$$

$$u \to u_G = -\frac{g'}{f}\frac{\partial h}{\partial y}. \tag{7}$$

Equations (4) and (5) can be solved using Ekman theory [see, e.g., *Cushman-Roisin*, 1994, p. 66; *Darelius*, 2008], for which the velocity in the directions along (u) and across (v) the channel are given by

$$u_e(z) = u_G\left(1 - e^{-\frac{z}{2\delta}}\cos(z/2\delta)\right) - v_G e^{-\frac{z}{2\delta}}\sin(z/2\delta), \tag{8a}$$

$$v_e(z) = u_G e^{-\frac{z}{2\delta}}\sin(z/2\delta) + v_G\left(1 - e^{-\frac{z}{2\delta}}\cos(z/2\delta)\right), \tag{8b}$$

where $\delta = \sqrt{\upsilon/f}$ is the Ekman layer thickness, u_G and v_G are the geostrophic velocities given by equations (6) and (7) in the interior, and it has been assumed that $h \gg \delta$. (We note that often a different definition of $\delta = \sqrt{2\upsilon/f}$ can be found in the literature [e.g., *Cushman-Roisin*, 1994].) Equations (8a) and (8b) have been plotted in Figure 2 for $u_G = 0.07$ m s^{-1}, $v_G = -0.01$ m s^{-1} and three different values of f. As can be seen, far above the boundary layer the velocity approaches the geostrophic velocities, and in the boundary layer the velocity rotates and decreases exponentially to zero. For $v_G \ll u_G$ the maximum value of $v(z)$ is $v_{MAX} = \frac{u_G}{\sqrt{2}}e^{-\frac{\pi}{4}} \approx 0.3u_G$, approached at $z \approx \frac{\pi\delta}{2}$. The mean velocity in the Ekman boundary layer is $v_{MEAN} \approx 0.1\ u_G$. The boundary layer thickness δ is indicated by thin horizontal lines in Figure 2. The net transport across the channel is found by vertical integration of equation (8b) from the bottom ($z = 0$) to the top of the dense layer ($z = h$), to give

$$\int_0^h v(z)dz = hv_G + \delta(u_G - v_G), \tag{9}$$

where we have used a standard result from Ekman theory, namely, that the transport in the Ekman boundary layer is given by $\delta(u_G - v_G)$ when $h \gg \delta$ (which will be used for the rest of the theory). Classical Ekman theory pertains to the flow over a solid boundary, but there are many examples of observations of interfacial Ekman layers, [e.g., *Darelius*, 2008; *Sherwin*, 2010]. The basic dynamics are the same, although the thickness of the layer may be greater than in the bottom boundary layer. The interfacial stress gives rise to an Ekman layer next to the interface, with the Ekman transport directed to the left of the main flow direction in the Northern Hemisphere (looking downstream). By vertical integration across the interfacial Ekman layer an expression similar to equation (9) is obtained. The net across-channel transport in the presence of both an interfacial and a benthic Ekman layer is hence given by

$$\int_0^h v(z)dz = hv_G + 2\delta(u_G - v_G), \tag{10}$$

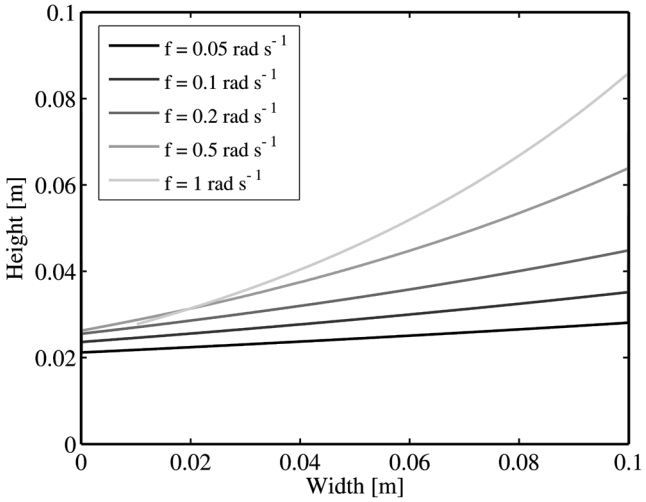

Figure 3. Calculated position of the interface in the channel after equation (13) for varying Coriolis parameter f.

where the factor 2 comes from the effect of including both boundary layers. We note that the δ here is still the viscous Ekman boundary layer, and will discuss the possible influence of a turbulent boundary layer later. When the Ekman boundary layers meet the vertical sidewalls the horizontal flow will be transported vertically within Stewartson boundary layers [*Duck and Foster*, 2001] and then returned to the interior flow. Provided there is no net transport across the channel the horizontal flow in the geostrophic interior balances the flow in the Ekman boundary layer, so that

$$h\mathrm{v}_G + 2\delta(u_G - \mathrm{v}_G) = 0. \tag{11}$$

Using equations (6) and (7), equation (11) can be rewritten as

$$\frac{\partial h}{\partial y} - s\frac{h}{2\delta} = -s, \tag{12}$$

which gives a solution for the position of the interface across the width of the channel as

$$h(y) = Ce^{\frac{sy}{2\delta}} + 2\delta. \tag{13}$$

In equation (13), C is a constant of integration with units of length that must be determined by a boundary condition. If we use the along-channel transport Q as the boundary condition (assuming that the dense layer is thick compared to the Ekman layer and $v_G \ll u_G$) we get

$$Q = \int_0^W hu_G\, dy = \int_0^W h\frac{g'}{f}\frac{\partial h}{\partial y}dy, \tag{14}$$

or using equation (13),

$$\begin{aligned} Q &= \frac{1}{2}\frac{g'}{f}\int_0^W \frac{\partial}{\partial y}(h^2)dy \\ &= \frac{1}{2}\frac{g'}{f}\left[h^2(W) - h^2(0)\right] \\ &= \frac{1}{2}\frac{g'}{f}\left[C^2\left(e^{\frac{sW}{\delta}} - 1\right) + 4\delta C\left(e^{\frac{sW}{2\delta}} - 1\right)\right]. \end{aligned} \tag{15}$$

From equation (15) we can express C in terms of Q. For most cases, in particular for high rotation rates, $\delta \ll h$ and the relationship between C and the volume flux Q is given by

$$C = \sqrt{\frac{2fQ}{g'}\frac{1}{\left(e^{\frac{sW}{\delta}} - 1\right)}}. \tag{16}$$

Figure 3 shows the interface for various rotation rates, looking downstream. In order to compare this expression for h with equation (3) we can determine $\Delta h = h(W) - h(0)$ using equation (13). The mean along-channel velocity U is given by the volume flux divided by the cross-sectional area A of the flow,

$$U = Q/A, \tag{17}$$

where the area is calculated using equation (13),

$$\begin{aligned} A &= \int_0^W h(y)\cdot dy = \int_0^W \left(Ce^{\frac{sy}{2\delta}} + 2\delta\right)\cdot dy \\ &= 2\frac{\delta}{s}\left(e^{\frac{sW}{2\delta}} - 1\right)\sqrt{\frac{Q}{\frac{g'}{2f}\left(e^{\frac{sW}{\delta}} - 1\right)}} + 2\delta W, \end{aligned} \tag{18}$$

and equation (16) has been used to define C. The mean downstream geostrophic velocity $\overline{u_G}$ will be referred to as U in the rest of the manuscript so that meaningful comparison can be made with the nonrotating environment.

3. Method

[12] The physical experiments were carried out on a computer-controlled rotating platform with a diameter of 1 m. The rotation rate was varied from $f = -1$ to $f = 1$ rad s^{-1} (including $f = 0$) to represent a range of different latitude systems. All experiments were conducted in a 1.85 m × 1.0 m × 0.35 m rectangular tank that was placed on the rotating platform (Figure 4). Inside this tank a channel model was placed and the tank was filled with tap water up to a level of approximately 0.30 m, so that the entire channel system was submerged by approximately 0.1 m at the inflow point. The channel model had a constant, rectangular cross-sectional shape with a width of 0.1 m and a height of 0.08 m. The length of the straight channel was 0.6 m and was elevated 0.12 m above the tank floor. When the density current leaves the channel the dense water flows into the sump region below the channel, which restricts the influence of gravity current reflections from the sides of the tank. In order to have a constant velocity of the inflow the saline water passed through a 0.10 m thick diffuser made of drinking straws and foam to damp any irregularities in the inflow velocity. The slope of the channel axis s was 1:50.

[13] In the experiments the turbidity current was modeled by a dense saline mixture as in previous studies [e.g., *Keevil et al.*, 2006; *Imran et al.*, 2007; *Islam et al.*, 2008] that have used saline gravity currents to gain insight into the flow field and secondary circulations in turbidity currents. The justification for this is that the dynamics of large-scale non-depositional turbidity currents are similar to density currents. The density contrast was generated with salt, and

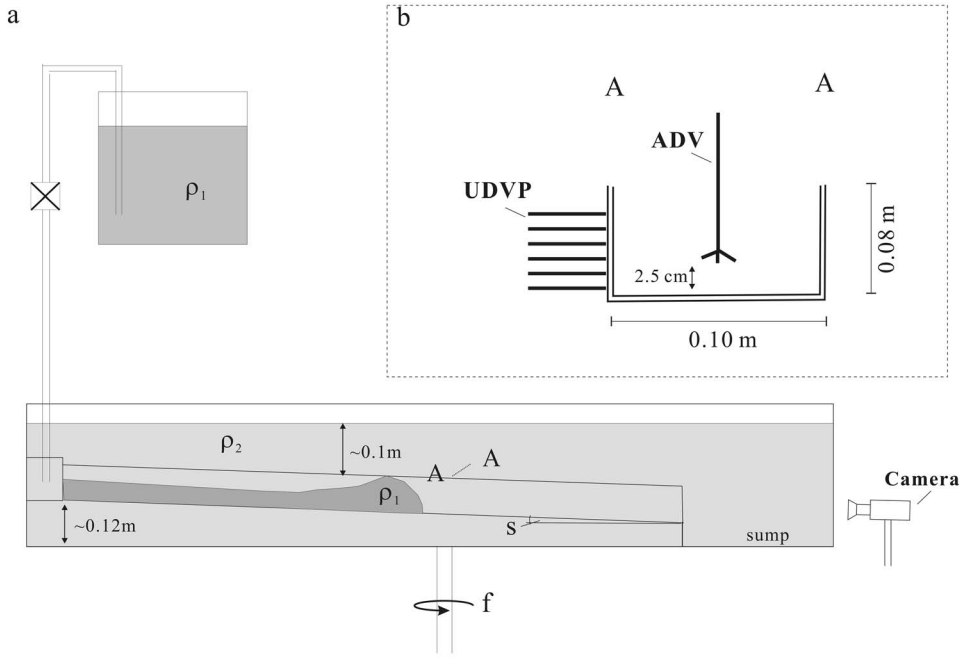

Figure 4. (a) Layout of the experimental setup. The velocity of the density currents was measured approximately 50 cm from the inflow at the upstream end of the channel model. (b) Position of the UDVP and ADV used for the measurements.

30 L of the saline mixture was pumped in at the upstream end of the straight channel section using a pump with a constant discharge of $Q = 16$ L/min, so that each flow lasted for about 120 s after the pump was turned on and the current entered the channel model. The excess density was 1%, giving a density for the saline current of 1010 kg m^{-3}. The tank was spun up for at least 30 min in order to achieve solid body rotation of the water, after which the experiment was initiated. In order to visualize the density current and the slope of the density interface blue food dye was added to the mixture in some experiments.

[14] The across-stream and along-stream velocities were measured at a distance of 0.5 m from the flow diffuser at the start of the channel. Two different acoustic velocity instruments were used: a Metflow ultrasonic Doppler velocity profiler (UDVP) and a Nortek acoustic Doppler velocimeter (ADV). Arrays of UDVPs have been frequently used in geometrically similar nonrotating experiments [e.g., *Best et al.*, 2001; *Corney et al.*, 2006; *Peakall et al.*, 2007]. An array of UDVP probes is ideal for making transverse measurements of the flow. Each UDVP probe can record single-component velocity data along a profile of 128 points along the axis of the ultrasound beam at a frequency of 4 Hz. Vertical velocity profiles were obtained from an array of 6 transducers to monitor the velocity at heights of 0.5, 1.5, 2.5, 3.5, 4.5 and 5.5 cm above the bottom (Figure 4b). Representative values were obtained by averaging the velocities over 30–35 s, starting immediately after the head of the current had passed the instrument (Figure 5).

[15] The second instrument was a Nortek ADV. This can sample simultaneously three components of velocity at frequencies up to 200 Hz, but only measures at a single point, so is a good complement to the UDVP. The ADV consists of one transmitter and three receivers which are slanted at 30° from the axis of the transducer and focus on a common sample volume of 80 mm^3 that is 50 mm away from the probes [*Voulgaris and Trowbridge*, 1998]. This ensures nearly nonintrusive flow measurements within the flow field of the current. The velocity components measured by the ADV were recorded in the center of the channel, 2.5 cm above the bottom at a frequency of 50 Hz (Figure 4b). The data were taken over the same sampling interval over which the UDVP data was averaged.

[16] In order to measure the interface position, a digital camera was used. In those experiments blue food dye was added to the salt water. The camera was mounted on the table looking upstream so that the thickness of the current and slope of the interface could be measured (Figure 4a).

4. Results

4.1. General Observations

[17] The aspects of the flow that have been analyzed are the flow velocity U of the interior bulk flow (measured with the ADV), the secondary flow cells (measured with the UDVP) and the deflection of the density interface (photographs).

[18] In the absence of rotation ($f = 0$ rad s^{-1}) the front of the dense current formed a head with the typical overhanging nose that covered the whole cross section of the channel. Behind the head the density current was significantly thinner, but the flow still occupied the whole channel width. After the passage of the head the flow conditions remained fairly constant. A small amount of mixing of ambient water into the current was noticed through the more transparent color at the upper interface. Vertical velocity profiles from several experiments with different values of the Coriolis parameter are shown in Figure 5 together with the point ADV measurements. The velocity profiles show

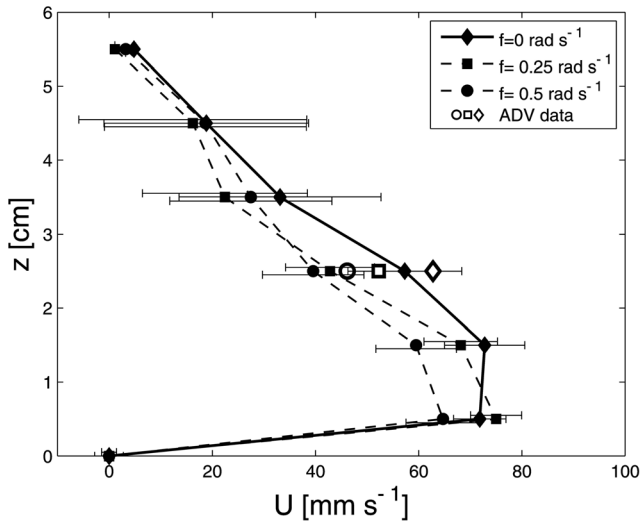

Figure 5. The time-averaged horizontal velocity plotted at different heights above the bed for three different rotation rates. These velocities were measured using the UDVP, and the error bars depict the standard deviation over the 30 s measurement period. Most of the volume flux of the density current is between 0.5 and 4 cm above the bottom. Hence, the point measurements with the ADV were taken at 2.5 cm above the bottom, to represent the significant velocities between 0.5 and 4 cm. This region of the flow best represents the geostrophically adjusted velocity u_g used in the theory section, for example, equations (7)–(14). The open markers showing the ADV data are taken at the same rotation rates as those for the closed markers for the UDVP data; for example, diamonds reflect a Coriolis parameter $f = 0$ rad s^{-1}.

the typical "bullet nose" profile [*Middleton*, 1993; *Kneller and Buckee*, 2000] with the maximum velocity close to 0.5–1 cm above the bottom. Within the bottom boundary layer the velocity increases nonlinearly between the base and the velocity maximum U_{max} as also observed by *Kneller et al.* [1999]. Above the velocity maximum the velocity decreases continuously to $U < 0.02$ m s^{-1} at 5.5 cm above bottom. On the basis of these profiles, the point measurements using the ADV were positioned 2.5 cm above the bottom, approximately representative of the mean downstream velocity. As can be seen in Figure 5 there is a favorable agreement between the UDVP measurements and the ADV measurements, which later were used to determine U.

[19] In the experiments with rotation the formation of the head and its transition to the body with a distinct thinning of the flow was less obvious, as the gravity current was pushed toward the wall after it had entered the channel. With positive f the currents were deflected to the right-hand side of the channel (looking downstream) and for negative Coriolis parameter ($-f$) to the left-hand side. This deflection became greater as the rotation rate increased. The propagation speed of the gravity currents was also observed to decrease significantly as the rotation rate increased. In the nonrotating experimental gravity currents shown in Figure 5, the mean velocity averaged over the entire thickness was approximately $U_{mean} = 0.04$ m s^{-1}. This flow had a thickness of approximately $h = 0.06$ m so that the Froude number was $Fr = U_{mean}/\sqrt{g'h} = 0.52$. Such a Froude number is broadly similar to many previous experimental observations of gravity currents where $0.2 < Fr < 1.3$ [*Garcia and Parker*, 1993; *Kneller et al.*, 1999; *Baas et al.*, 2005; *Gray et al.*, 2006]. Flows with such small Froude numbers are also expected to have very low interfacial entrainments rates [*Wells and Wettlaufer*, 2007; *Wells and Nadarajah*, 2009; *Wells et al.*, 2010]. The flow had a Reynolds number of $Re = 2400$ where $Re = U\,h/\nu$, where ν is the molecular viscosity. The value of Re indicates that the flow was turbulent and can be compared to other experimental gravity currents such as those from *Kneller et al.* [1999], *Amy et al.* [2005], or *Davies et al.* [2006] with similar Reynolds numbers where the flow was turbulent.

[20] The distance over which the flow is expected to adjust geostrophically is on the order of the internal Rossby radius of deformation defined as $R_{def} = (g'h)^{1/2}/f$ [e.g., *Darelius*, 2008; *Wells*, 2009]. For the rotating gravity currents used in our experiments the value of R_{def} is about 0.4 m for low rotation rates of $f = 0.1$ rad s^{-1}. For higher rotation rates the radius of deformation decreases rapidly. As all of the velocity measurements were obtained 0.5 m from the inflow point we expect that the flow will have reached geostrophic conditions.

4.2. Observations of Downstream Velocity *U*

[21] The downstream velocities measured with the ADV for different rotation rates are plotted in Figure 6 and compared to the mean velocity based on the theory incorporating Ekman dynamics (e.g., using equations (17) and (18)) which predicts a significant decrease of the downstream velocity between small and large Coriolis parameter f. The error bars indicate the standard deviation in the averaging period. The experiments reveal that for $f < 0.2$ rad s^{-1} the velocity is not significantly influenced by rotation as the velocity remains relatively constant at $U \sim 0.07$ m s^{-1}, which is close to the velocity computed on the basis of the density difference and a constant Froude number. As f increases the measured downstream velocity decreases. At large f the downstream velocities are up to 40% smaller than for the nonrotating case ($f = 0$). The experimental data show good agreement with the theory using Ekman boundary layer dynamics (equations (17) and (18)).

[22] In Figure 6 there is a slight offset in the downstream velocity between small positive and negative Coriolis parameter (e.g., between $f = 0.1$ and 0.25 rad s^{-1}). We can attribute this velocity difference mainly to two reasons: the alignment of the measuring device might not have been exactly at the centerline so that the maximum speed of current was not captured perfectly during those experiments. Second, owing to the experimental setup at the inflow point those currents were not entirely uniform and more pronounced at either the right-hand or left-hand side of the channel so that the maximum flow velocity was offset to the position of the measuring device. However, we can consider those differences as negligible as the overall data set reveals a distinct and consistent trend, with symmetry at large f (small Ro).

[23] The analytical expressions (equations (10) and (18)) are based on purely laminar flow conditions [*Wåhlin*, 2002; *Darelius*, 2008]. However, a large Reynolds number of $Re = 2400$ suggests that the currents are rather turbulent than

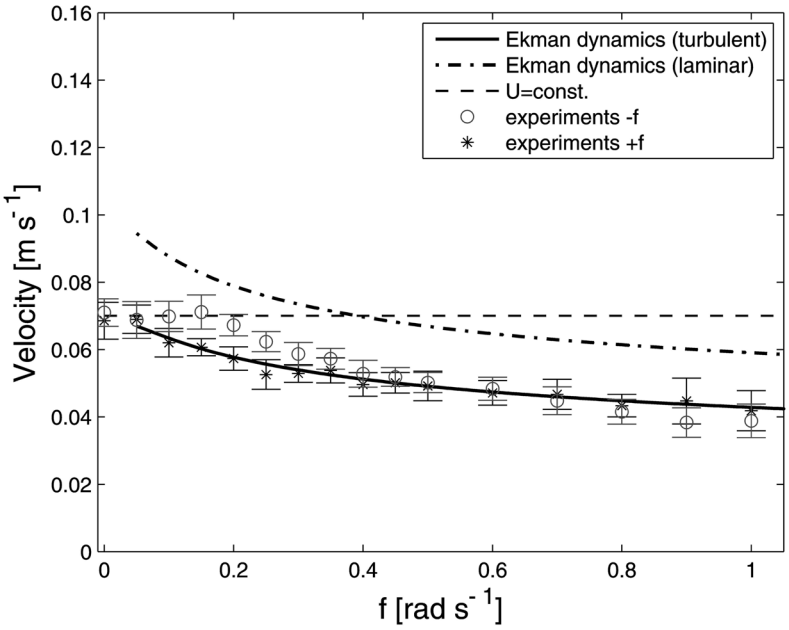

Figure 6. Dependence of the mean downstream velocity U with varying Coriolis parameter f. The graph shows mean velocity U based on the initial Froude number and U calculated using equations (17) and (18) with a turbulent and a laminar boundary layer and direct ADV measurements. The ADV data were taken at a height of 2.5 cm above the base and in the middle of the channel approximately 0.5 m away from the injection point.

laminar. In both the turbulent and laminar flows, the thickness of the boundary layers represents the length scale over which friction is important. This thickness can be estimated by rearrangement of the Ekman number, which is defined as $Ek = \nu/\Omega H^2$ [*Cushman-Roisin*, 1994], where H is a characteristic vertical length scale. If the Ekman number is of order 1, then frictional influences are important so that $H \sim \sqrt{\nu/\Omega}$. The expression for the turbulent boundary layer thickness comes from a consideration of the turbulent viscosity. For instance, in Figure 2 the theory ($\delta = \sqrt{\upsilon/2f}$) predicts thicknesses of the laminar boundary layer of order 0.1 cm. As will be demonstrated in section 4.3 and 4.4 the observations of the experimental currents suggest that there are larger boundary layers, in particular turbulent mixing with the ambient water at the upper boundary layer led to a thick interfacial boundary layer (Figure 10b). When comparing our theory using Ekman dynamics (equations (17) and (18)) with the observations of velocities and interface slope, we make the simple assumption that the turbulent Ekman boundary layers are thicker than the laminar Ekman boundary layers. This is consistent with the scaling of a turbulent boundary layer, which can be defined in terms of the turbulent velocity scale as $\delta^* = 0.4\frac{u^*}{f}$ [*Weatherly and Martin*, 1978], where u^* represents the friction velocity. The friction velocity can be defined in terms of the mean velocity as $u^* = \sqrt{C_D}U$. Thus with f = 0.25 rad s^{-1}, where the velocity U is 0.06 ± 0.005 m s^{-1} (Figure 6), a drag coefficient of C_D = 0.003 [*Umlauf and Arneborg*, 2009a] implies u^* = 0.0032 m s^{-1} so that the turbulent Ekman boundary layer is $\delta^* \sim 0.4$ cm, which is approximately 2.5–3 times larger than the thickest theoretical laminar boundary layer thickness of δ = 0.14 cm (black dashed line Figure 2). Empirically we find the best fit to our experimental data where we use $\delta^* = 1.7\delta = 1.7\sqrt{\nu/2f}$. This is a reasonable value as it is larger than the laminar model and smaller than turbulent scaling which can overpredict the thickness in strongly stratified fluids [*Weatherly and Martin*, 1978]. Using a thicker turbulent Ekman boundary layer thickness yielded velocities that were significantly smaller than with a laminar boundary layer. and are in much better agreement with the experimental data in Figure 6. We use this estimated turbulent boundary layer thickness in equation (18) and in the rest of the manuscript so that more meaningful comparison can be made with the experimental density currents.

[24] The experimental velocity data can be expressed in a more general way by the use of a dimensionless Rossby number Ro and the Froude number Fr, which are plotted in Figure 7. We note that we now use the averaged geostrophic velocity of the interior of the current (from Figure 6) to define Fr. For $Ro < 2$ there is generally a good agreement between the theory using Ekman boundary layer dynamics (equations (17) and (18)) and the measured velocities. The poorer agreement for $Ro > 2$ suggests that equations (17) and (18) are less applicable for large Ro. This is expected as we assumed that $f \gg 0$ rad s^{-1}, in order for the flow to be geostrophically adjusted, and for the Ekman boundary layers to be fully developed. Owing to the small velocity differences between small positive and negative Coriolis parameter f (Figure 6), we observe a slight asymmetry in the Froude numbers (the normalized velocity) when the flow is not strongly rotationally controlled, that is, for $Ro > 2$. On the basis of the experimental results in Figures 6 and 7, we conclude that only for $Ro < 2$ does the Coriolis effect become significant for our experimental gravity currents. Such a threshold is consistent with oceanographic literature

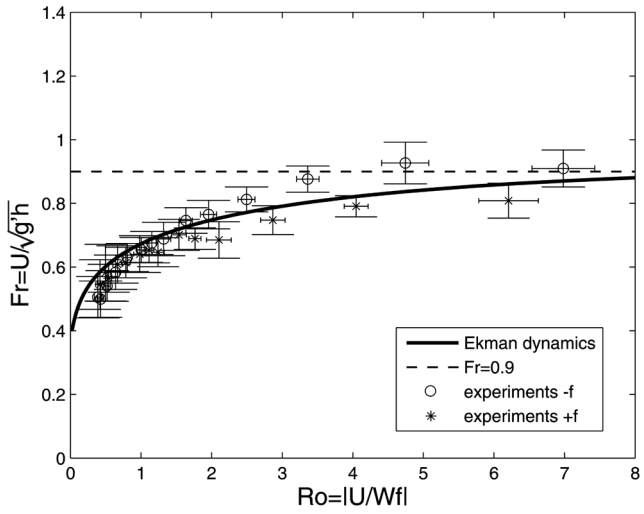

Figure 7. Relation between Rossby number *Ro* and the Froude number *Fr* for the channel model with varying Coriolis parameter *f*. *Ro* and *Fr* (using $h = 0.06$ m from Figure 5) are based on the measured mean velocity *U* (in the interior of the flow), the calculated mean velocity *U* using equations (17) and (18) (solid line), and *U* based on the assumption of a constant velocity with $Fr = 0.9$ (dashed line).

where *Ro* of order 1 is usually the criterion when currents start to feel the effect of rotation [e.g., *Nof*, 1996; *Wells*, 2009].

4.3. Slope of the Interface With Changing *f*

[25] The strong influence of the Coriolis force on the lateral density interface can be seen in Figure 8. The photographs show the shape of the across-stream interface for $Ro \sim \infty$ ($f = 0$) and $Ro = 0.83$ ($f = \pm 0.6$ rad s^{-1}) looking upstream. For the case without rotation ($f = 0$ rad s^{-1}, Figure 8b) the density interface is horizontal. Those conditions, where *f* is almost zero, would be relevant to large-scale turbidity currents that occur in areas close to the equator, or for which the scales are such that $Ro > O(1)$. With smaller *Ro*, illustrated in Figure 8a (for $f = +0.6$ rad s^{-1}) and Figure 8c for ($f = -0.6$ rad s^{-1}), a significant deflection of the slope of the across-stream interface can be observed. For a positive Coriolis parameter (Northern Hemisphere), a deflection of the current to the right-hand side (looking downstream) can be seen. For a negative *f* (Southern Hemisphere), the flow is deflected to the left-hand side of the channel. The height difference of the interface between the left and the right channel wall is negligible for an infinite *Ro*, but for $Ro = 0.83$ the difference is about 4 cm, which accounts for more than half of the depth of the nonrotating gravity current. This tilt of the interface due to the rotation was also observed in the low Reynolds number experiments by *Darelius* [2008] and with a numerical model by *Imran et al.* [1999].

[26] Figure 9 shows the relation between *Ro* and the observed deflection Δh of the interface, normalized by the current thickness *h*. The deflection of the interface is defined as the height difference between the left-hand and right-hand sides of the interface at the channel walls. The experimental results demonstrate that with decreasing *Ro* the deflection increases. In addition, Figure 9 compares the experimental results with the theoretical approaches to define the deflection according to the theory of *Komar* [1969] expressed in equation (3) (where $\Delta h/h = 1/Ro$) and the theory involving

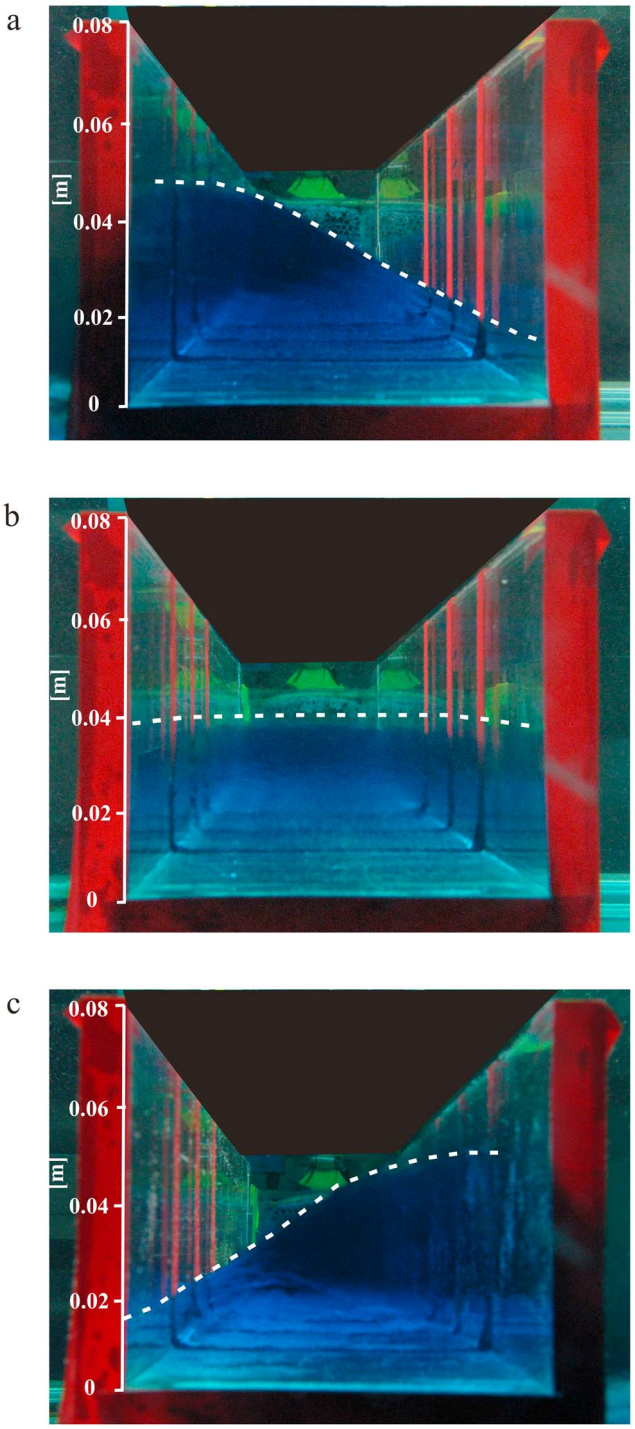

Figure 8. Deflection of the interface of the density currents for (a) $Ro = 0.83$ (with $f = +0.6$ rad s^{-1}), (b) $Ro = \infty$ (with $f = 0$ rad s^{-1}), and (c) $Ro = 0.83$ (with $f = -0.6$ rad s^{-1}). Note that the perspective is upstream, and hence a deflection to the left-hand side means a deflection to the right-hand side from the downstream perspective.

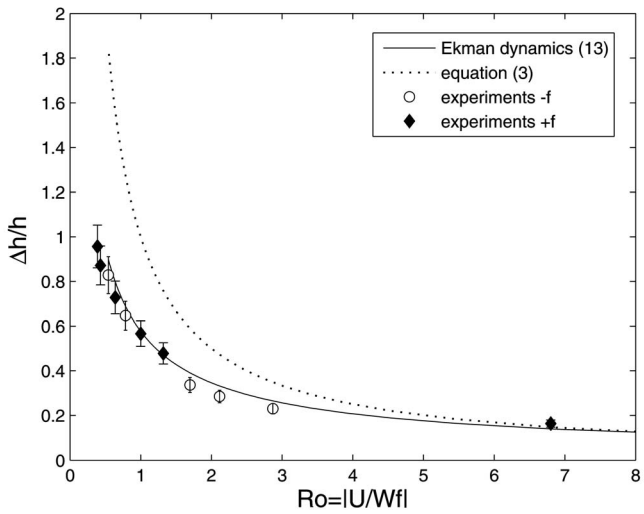

Figure 9. Comparison of the deflection Δh and Ro for varying Coriolis parameter f after equation (3), Ekman boundary layer dynamics following equation (13), and the measured height differences. The Δh is normalized by the current thickness h = 0.06 m (Figure 5) and reflects the difference of the interface between the left-hand and right-hand channel walls. Error bars of the experimental data depict a variance of 10% due to a measuring inaccuracy based on a blurry upper interface.

Ekman boundary layers of equation (13), respectively. For small Ro the measured height difference is approximately 50% smaller than predicted by equation (3) and there is generally a better agreement with the theory that used turbulent Ekman boundary layer dynamics. The lack of viscous effects and Ekman boundary layers in equation (3) tends to overestimate the slope of the interface when rotation is important as the velocity is also overestimated (Figures 6 and 7).

4.4. Secondary Flow Cells and Across-Stream Velocities

[27] The secondary circulation patterns in the channel are illustrated in Figure 10 for various Rossby numbers. Without rotation there are two adjacent flow cells in the channel that spin in opposite directions, with a flow convergence at the surface and divergent flow at the bottom of the density current (Figure 10a). This is essentially the same as the classic "helicoidal flow" that was first observed in rivers at the end of the 19th century, and reported in open channel flows [e.g., *Rhoads and Welford*, 1991; *Colombini*, 1993]. In a rotating density current the secondary circulation changes dramatically, as demonstrated in Figures 10b and 10c for Ro = 2.4 ($f = \pm 0.25$ rad s^{-1}). The positive rotation leads to a deflection of the current to the right-hand side (Figure 10b) and a corresponding interior flow v_G with maximum velocities up to 0.005 m s^{-1} toward the right-hand wall (looking downstream). This interior flow is bordered by two return flows v_e at the upper interface and the bottom of the density current, which are the Ekman boundary layers. The maximum velocities of these return flows are approximately $v_e = 0.015 \pm 0.005$ m s^{-1} and hence larger than the interior flow toward the wall. Using equations (8a) and (8b) the magnitude of the velocities in the Ekman boundary layer can also be estimated. As the mean downstream velocity for $f = 0.25$ rad s^{-1} is $U = 0.06$ m s^{-1} we predict that the mean velocity in the Ekman boundary layer is $v_e = 0.017$ m s^{-1}. This theoretical velocity conforms to the observed velocity in Figure 10b where the transverse velocities have a magnitude $v_e = 0.015 \pm 0.005$ m s^{-1} and are approximately 25% of the downstream velocity U.

[28] As the bulk flow v_G in the interior toward the right wall of the channel (looking downstream) occupies about 60% of the depth of the current (near the right wall of the channel), the return flows v_e that occur in the thinner Ekman boundary layers have a higher velocity than in the interior bulk flow (Figures 2 and 10) in order for the integral of the cross-stream velocity to be zero. When our experimental measurements of the transverse velocity were integrated over the whole depth of the density current, we found an almost balanced relation between the interior flow and the opposite velocities in the boundary layers. For larger f this balance between v_G and v_e is even more prominent as the Ekman boundary layers tend to get thinner (see section 2.1) while the interior flow expands further over the whole thickness. This is accompanied with smaller bulk velocities v_G in the interior and faster return flows v_e in the boundary layers. Figure 10c illustrates basically the same flow field as that in Figure 10b, but for negative f and hence mirrors the flow field of Figure 10b. Similar flow fields to those shown in Figure 10 have been described by *Johnson and Ohlsen* [1994], *Davies et al.* [2006], and *Darelius* [2008] from experiments in rotating fluids. Analogous secondary flow patterns have also been reported in several natural gravity currents, for example, in the Faroe Bank Channel [*Johnson and Sanford*, 1992; *Fer et al.*, 2010], in the Ellet Gully [*Sherwin*, 2010], and in the Baltic Sea [*Umlauf and Arneborg*, 2009a, 2009b].

[29] The magnitude of the secondary flows can be estimated from the geostrophic velocities by rearranging equations (6) and (7). Division of equation (6) by equation (7) gives an estimate of the ratio of the interior transverse velocity v_G to the mean downstream velocity U as $v_G/U = s/(dh/dy)$. In our experiments the downstream slope of the channel s was constant, whereas the cross-channel slope of the interface dh/dy increases for decreasing Ro (Figure 9), so that v_G/U should also decrease with Ro. Figure 7 showed that the theory incorporating Ekman boundary dynamics appeared to be particularly suitable for $Ro < 2$. Figure 11 depicts the measured values of the observed relation $s/(dh/dy)$ for $Ro < 4$. With an increasing deflection, the geostrophic interior of the flow becomes proportionally thicker, while the Ekman boundary layers decrease in thickness, which results in a reduction in the velocity v_G and consequently a reduction of the ratio v_G/U. For large rotation rates or $Ro < 0.5$ the ratio v_G/U is approximately 0.3. Figure 11 shows a partial regression line from which the relationship $U = 0.5\ sW^2 f/\Delta h$ can be derived. This simple empirical relationship could be used as a first-order approximation to determine the mean downstream velocity U of a turbidity current if the levee height difference and the slope of the submarine channel system is known.

[30] There has been a considerable effort recently to look at the secondary circulations in turbidity currents flowing in submarine channels, in particular in the bends of sinuous

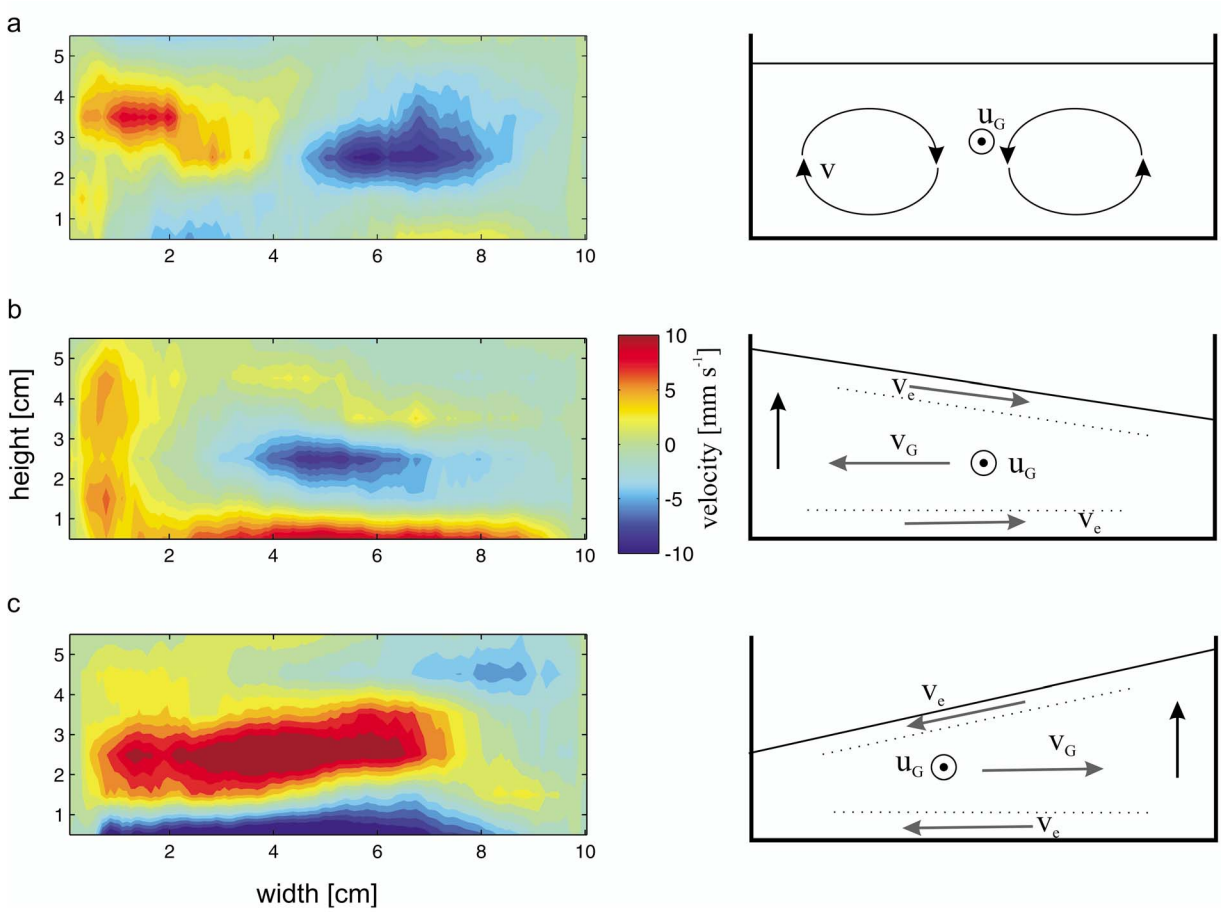

Figure 10. Across-stream velocities for the experimental flows in the submarine channel (looking upstream) measured with the UDVP: (a) $Ro = 2.4$ (with $f = 0.25$ rad s^{-1}), (b) $Ro = \infty$ (with $f = 0$ rad s^{-1}), and (c) $Ro = 2.4$ (with $f = -0.25$ rad s^{-1}). The sense of the rotation is sketched on the right-hand side. Note the upwelling mechanism denoted by the upward directed arrow in the sketches in Figures 10b and 10c.

channels [*Keevil et al.*, 2006; *Islam et al.*, 2008; *Islam and Imran*, 2008; *Straub et al.*, 2008]. In channel bends, the curvature-induced centrifugal acceleration of the flow balances an inwardly directed radial pressure gradient leading to secondary flows that are of order of 10% of the mean flow. It is worth noting that the secondary flows driven by Coriolis effects have a similar magnitude to these previously studied flows but quite a different internal structure.

5. Discussion

[31] An understanding of flow dynamics and sediment transport processes in submarine channels is essential to interpret and analyze their morphology and architecture and to develop process models [e.g., *Peakall et al.*, 2000; *Pirmez and Imran*, 2003]. The growth of channel levee systems is thought to arise from extensive overbank flow and overspill, on the basis of direct observations of overbank flow [*Normark and Dickson*, 1976; *Normark*, 1989], and from observations of the grain size distribution taken from silt and fine-sand beds on levee crests [*Hesse et al.*, 1987; *Hiscott et al.*, 1997]. The height of turbidity currents can extend vertically beyond the channel depth up to a factor of 4 [*Normark*, 1989] and fine-grained sediment in this upper

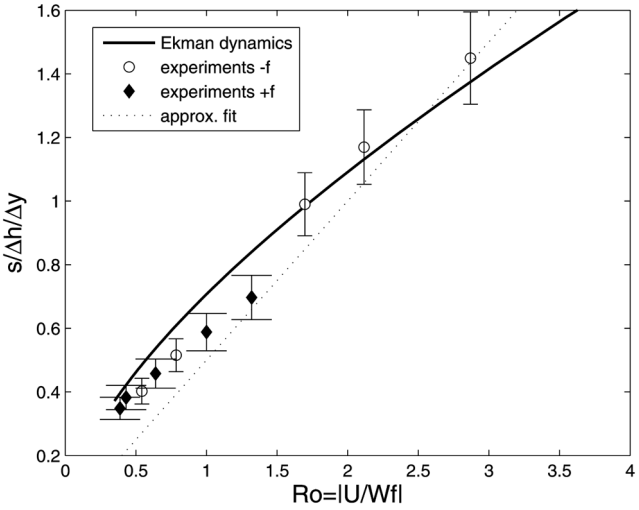

Figure 11. Relation between $s/(dh/dy)$ and Ro for varying Coriolis parameter f. The graph compares experimental data and the Ekman boundary layer dynamics calculated after equation (13).

part residing above the channel can spread laterally and be deposited on the overbank surface [*Straub et al.*, 2008]. Hence, in straight channel sections finer sediments are usually found along channel levees rather than inside the channel and this continuous overspill accounts for levees growth along submarine channels, for example, in the NAMOC [*Klaucke et al.*, 1998] or the Amazon channel [*Pirmez and Imran*, 2003]. In channel bends, however, the levee deposits can also consist of coarse-grained sediments that are upwelled by centrifugal forces. These flow dynamics in channel bends have been studied extensively in nonrotating sinuous submarine channels [e.g., *Corney et al.*, 2006; *Keevil et al.*, 2006; *Peakall et al.*, 2007; *Straub et al.*, 2008]. Channel bend levees at the outer bank result predominantly from overspill deposition caused by centrifugal forces, and the secondary flow cells. The deflection of the interface and the movement of sediment by the secondary circulation, leads to an outer bank upwelling toward the overbank region and promotes subsequent growth of high outer bank channel levees [*Corney et al.*, 2006; *Straub et al.*, 2008].

[32] Our results show that strong secondary circulations are present in straight channel sections for $Ro < 2$ ($f > 0.25$ rad s^{-1}) owing to the interaction of Coriolis force and pressure gradient force. A continuous deposition of sediments that are carried by these secondary circulations in turbidity currents could lead to the asymmetry between right-hand and left-hand levee banks, which has been described for several submarine channel systems in the Northern and Southern Hemispheres [*Menard*, 1955; *Carter and Carter*, 1988; *Klaucke et al.*, 1997]. These secondary flows could contribute to overbanking in straight channel section where the centrifugal force is absent. The secondary circulation consists of an interior flow toward the right-hand side of the channel (looking downstream) in the Northern Hemisphere and a return flow along the density interface (Figure 10b). Hence this secondary flow cell could lead to an upwelling of sediment at the right-hand side of the channel and promote the growth of the right-hand levee by continuous deposition (denoted by the vertical arrow in Figure 10b). This upwelling is a similar mechanism that has been reported in channel bends without rotation, where there was pronounced levee formation on the outer bends of submarine channels [*Corney et al.*, 2006; *Keevil et al.*, 2006]. In a rotating system, we hypothesize that similar upwelling of sediment, driven by the observed secondary flows, causes a constantly larger sediment flux toward the right-hand side of straight channel sections, leading to a consistent increase in levee heights on the right-hand side of submarine channels. This upwelling might also lead to deposition of coarser sediment which is usually transported at the base of the current onto the right-hand levee. Such deposition patterns and grain size distributions have been observed by *Straub et al.* [2008] driven by a similar mechanism with the superelevation and upwelling at an outer channel bend. In the Southern Hemisphere the negative Coriolis parameter forces this upwelling of sediments onto the left-hand side of the channel (looking downstream), leading to greater levee heights on the left-hand side of the channel (Figure 10c).

[33] In addition, the experiments showed good agreement with our theory (equations (13), (17)), and (18)) that incorporated Ekman boundary layer dynamics. In particular there was good agreement with the predicted reduction in downstream velocity, U, and for the magnitude of the cross-channel interface difference, Δh. Our theory agreed with our observations better than the theory of *Komar* [1969] in straight submarine channels. This is an important result, as the new theory can now be used as an analytical method to derive flow properties from field data of submarine channel systems.

[34] The experiments indicate that the transition between the regimes when the two different models should be used can be expressed in terms of the Rossby number so that the transition occurs approximately for $Ro = O(1)$. For example, in the NAMOC the right levee bank exceeds the left levee bank up to 100 m, so that the ratio between Δh to the entire depth D of the channel is often large with $\Delta h/D > 0.5$. The use of equation (3) for the NAMOC channel predicts downhill velocities between 0.1 and 1.06 m s^{-1} [see *Klaucke et al.*, 1997, Table 1]. The corresponding Rossby numbers for these velocities at a latitude 53° N are small ranging from 0.2–0.5. These small values of Ro indicate the Ekman boundary layer dynamics cannot be neglected in this system. At the equivalent Rossby number for our experimental analog in Figure 6, we found that the effective downhill velocity is over 30% smaller than obtained following equation (3). Hence, we conclude that the actual velocities in the NAMOC in straight channel sections are generally smaller than proposed by *Klaucke et al.* [1997] by a factor of 0.7.

[35] For smaller submarine channel systems such as the Navy fan in California, where the estimated downstream velocities in the narrow upper fan are of order 0.75 ms^{-1} [*Bowen et al.*, 1984] there would be large Rossby numbers of about 10–18, for a latitude 33.5° N and a width $W = 0.5$–1 km. Consequently in this channel rotation appears to be less important and no significant asymmetry of the channel banks has been reported in the upper fan valley. However, when the system widens toward the mid and lower fan system, from 3 km to 8 km, the velocities drop significantly to 0.12–0.3 m s^{-1} and $Ro < 1$ are obtained. In this region, *Bowen et al.* [1984] observed an asymmetry on the midfan with the right-hand side levee of the fan system (looking downstream) being up to 30 m higher than the left-hand side.

[36] Another example of a gravity current flowing in a submarine channel is the Mediterranean inflow into the Black Sea [*Flood et al.*, 2009]. Here a density current bearing a small amount of sediment, continuously flows through a submarine channel system. When the channel is on the inner shelf it has a width between 0.5 and 1 km and a depth of 10–35 m [*Flood et al.*, 2009]. For the velocity range of about 0.2–0.4 m s^{-1} [*Özsoy et al.*, 2001], the predicted Rossby numbers are in the range $Ro = 2$–5 suggesting that Coriolis forces will likely influence the secondary circulation of any gravity currents in this channel system. Specifically we would expect that the density interface tilts to the right-hand side, and any sediment will be deposited dominantly on the right-hand levee. However, owing to the lack of significant sediment load in the density current this system shows no prominent levee systems. On the basis of our results, we predict that the density interface would exhibit a tilt resulting in the interface being up to 5 m higher at the right-hand side (looking downstream). With a downstream velocity of 0.2–0.4 m s^{-1} we expect that the

mean velocity of the Ekman boundary layers will be of order 0.05–0.1 m s^{-1} and will be directed to the left-hand side of the channel looking downstream. At high discharge rates this might also lead to intensive overspill of dense saline water, which could build features like antidunes outside of the channel that have been observed and linked to overbank flow [*Flood et al.*, 2009].

[37] Near the equator the Coriolis parameter is small and any asymmetry in levee heights is expected to be less prominent compared to high latitudes. Nonetheless, the deep sea submarine channel system offshore of Trinidad and Tobago at latitude 10.5° displays a consistently higher right levee system, with cross-channel differences of up to 20 m. This asymmetry in the approximately 600 m wide and 200 m deep channel is attributed to the regional southward dip of the northeastern South American basin [*Wood and Mize-Spansky*, 2009]. Nonetheless, we note that for small downstream velocities, that are likely to occur in the upper portion of the velocity profile of a gravity current (as in Figure 5) Rossby numbers of order 1 can be obtained. Fine sediments transported as suspended load in the upper profile of a turbidity current [*Peakall et al.*, 2000] would predominantly be deflected to the right-hand side of the channel system. In this light, the observed asymmetry of up to 10% of the whole channel depth could also be attributed to Coriolis forces. It follows that thicker, slower and finer-grained turbidity currents could give rise to levees with more prominent asymmetry than thinner and faster, coarser-grained turbidity currents, even at low latitudes.

6. Conclusions

[38] This work demonstrated that the Coriolis force plays an important role in determining the velocity structure in gravity currents running through straight submarine channels. The frequently observed asymmetry in depositional elements in large-scale submarine channels, where the right-hand (left-hand) levee banks tend to be higher in the Northern Hemisphere (Southern Hemisphere), can be linked to the Earth's rotation and arising rotational effects on large-scale turbidity currents. In geological applications, the theory of *Komar* [1969] as expressed by equation (3) has been used to derive flow parameters from submarine channel systems. In contrast, oceanographic studies mostly include Ekman boundary layer dynamics to describe the characteristics of gravity currents in the ocean.

[39] The major findings of the analog model used in this paper were that the theoretical model using Ekman boundary layer dynamics is more accurate in describing the downstream velocity U and the interface tilt Δh for channels that have scales with Rossby numbers smaller than 2. In addition, it can be used to describe the secondary across-stream velocities v_G and v_e. The downstream velocity decreases significantly as the rotation rate increases, so that the theory after equation (3) overestimates the velocity by more than 30% for large rotation rates. Similarly, the theory of *Komar* [1969] overestimates the tilt of the interface by as much as 50%.

[40] Significant secondary circulations develop that are driven by Ekman boundary layer dynamics. Those flow cells promote an upwelling at the right-hand side of the channel (looking downstream) in the Northern Hemisphere and an upwelling at the left-hand side of the channel in the Southern Hemisphere which governs most likely sedimentation transport processes and the evolution of submarine channels.

[41] The Rossby number $Ro = |U/Wf|$, where U is the mean downstream velocity, W the channel width and f the Coriolis parameter, can be used to determine whether the rotational effects should be taken into account. The results show that particularly for $Ro < 2$ the flow properties are better reflected by the theory incorporating the Ekman boundary layers dynamics.

[42] In related work [e.g., *Cossu and Wells*, 2010] we have experimentally investigated the combined influence of centrifugal forces and Coriolis forces upon the secondary flow in channel bends. Generally we find that for small Rossby numbers Coriolis forces will lead to strong Ekman boundary layers, and that the secondary flows could look quite different from previous nonrotating studies [*Keevil et al.*, 2006; *Islam et al.*, 2008; *Straub et al.*, 2008]. In a curved channel, the downstream velocity is reduced compared to nonrotating experiments and the magnitude of any secondary flows is of the order 20% of the downstream velocity. If the Coriolis forces are sufficiently large, they can overwhelm the centrifugal forces and lead to strong flow asymmetries, so that in the Northern Hemisphere there can be more overbanking of the channel bends turning left rather than channel bends turning right.

[43] **Acknowledgments.** We gratefully acknowledge the support of Jeff Peakall, who loaned a Metflow UDVP system of the NERC-supported Sorby Environmental Fluid Dynamics Laboratory at Leeds University for the use in these experiments. The rotating table was built on a design generously provided by Karl Helfrich. Helpful conversations with Ilker Fer and Lars Umlauf are acknowledged. Mathew Wells received financial support from NSERC, the Canadian Foundation for Innovation and the Ontario Innovation Trust. Remo Cossu was partially supported in this work by a travel grant from the Centre for Global Change Science at the University of Toronto.

References

Amy, L. A., J. Peakall, and P. J. Talling (2005), Density- and viscosity-stratified gravity currents: Insight from laboratory experiments and implications for submarine flow deposits, *Sediment. Geol.*, *179*, 5–29, doi:10.1016/j.sedgeo.2005.04.009.

Baas, J. H., W. D. McCaffrey, P. D. W. Houghton, and C. Choux (2005), Coupling between suspended sediment distribution and turbulence structure in a laboratory turbidity current, *J. Geophys. Res.*, *110*, C11015, doi:10.1029/2004JC002668.

Benton, G. S., and D. Boyer (1966), Flow through a rapidly rotating conduit of arbitrary cross-section, *J. Fluid Mech.*, *26*, 69–79, doi:10.1017/S0022112066001095.

Best, J. L., A. D. Kirkbride, and J. Peakall (2001), Mean flow and turbulence structure of sediment laden gravity currents: New insights using ultrasonic Doppler velocity profiling, in *Particulate Gravity Currents*, edited by W. D. McCaffrey et al., pp. 157–172, Blackwell Sci., Malden, Mass., doi:10.1002/9781444304275.ch12.

Bowen, A. J., W. R. Normark, and D. J. W. Piper (1984), Modelling of turbidity currents on Navy Submarine Fan, California Continental Borderland, *Sedimentology*, *31*, 169–185, doi:10.1111/j.1365-3091.1984.tb01957.x.

Bruhn, C. H. L., and R. G. Walker (1997), Internal architecture and sedimentary evolution of coarse-grained, turbidite channel-levee complexes, Early Eocene Regencia Canyon, Espirito Santo Basin, Brazil, *Sedimentology*, *44*, 17–46, doi:10.1111/j.1365-3091.1997.tb00422.x.

Carter, L., and R. M. Carter (1988), Late Quaternary development of left-bank-dominant levees in the Bounty trough, New Zealand, *Mar. Geol.*, *78*, 185–197, doi:10.1016/0025-3227(88)90108-9.

Cenedese, C., and C. Adduce (2008), Mixing in a density-driven current flowing down a slope in a rotating fluid, *J. Fluid Mech.*, *604*, 369–388, doi:10.1017/S0022112008001237.

Cenedese, C., J. A. Whitehead, T. A. Ascarelli, and M. Ohiwa (2004), A dense current flowing down a sloping bottom in a rotating fluid, *J. Phys. Oceanogr.*, *34*, 188–203, doi:10.1175/1520-0485(2004)034<0188:ADCFDA>2.0.CO;2.

Chant, R. J., and R. E. Wilson (1997), Secondary circulation in a highly stratified estuary, *J. Geophys. Res.*, *102*, 207–215.

Chough, S., and R. Hesse (1976), Submarine meandering thalweg and turbidity currents flowing for 4,000 km in the Northwest Atlantic Mid-Ocean Channel, Labrador Sea, *Geology*, *4*, 529–533, doi:10.1130/0091-7613(1976)4<529:SMTATC>2.0.CO;2.

Colombini, M. (1993), Turbulence-driven secondary flows and formation of sand ridges, *J. Fluid Mech.*, *254*, 701–719, doi:10.1017/S0022112093002319.

Corney, R. K. T., J. Peakall, D. R. Parsons, L. Elliott, K. J. Amos, J. L. Best, G. M. Keevil, and D. B. Ingham (2006), The orientation of helical flow in curved channels, *Sedimentology*, *53*, 249–257, doi:10.1111/j.1365-3091.2006.00771.x.

Cossu, R., and M. G. Wells (2010), Coriolis forces influence the secondary circulation of gravity currents flowing in large-scale sinuous submarine channel systems, *Geophys. Res. Lett.*, *37*, L17603, doi:10.1029/2010GL044296.

Cushman-Roisin, B. (1994), *Introduction to Geophysical Fluid Dynamics*, Prentice-Hall, Upper Saddle River, N. J.

Darelius, E. (2008), Topographic steering of dense overflows: Laboratory experiments with V-shaped ridges and canyons, *Deep Sea Res., Part I*, *55*, 1021–1034, doi:10.1016/j.dsr.2008.04.008.

Darelius, E., and A. K. Wåhlin (2007), Downward flow of dense water leaning on a submarine ridge, *Deep Sea Res., Part I*, *54*, 1173–1188, doi:10.1016/j.dsr.2007.04.007.

Davies, P. A., A. K. Wahlin, and Y. Guo (2006), Laboratory and analytical model studies of the Faroe Bank Channel deep-water outflow, *J. Phys. Oceanogr.*, *36*, 1348–1364, doi:10.1175/JPO2917.1.

Droz, L., and D. Mougenot (1987), Mozambique upper fan: Origin of depositional units, *AAPG Bull.*, *71*, 1355–1365.

Duck, P. W., and M. R. Foster (2001), Spin-up of homogeneous and stratified fluids, *Annu. Rev. Fluid Mech.*, *33*, 231–263, doi:10.1146/annurev.fluid.33.1.231.

Emms, P. W. (1999), On the ignition of geostrophically rotating turbidity currents, *Sedimentology*, *46*, 1049–1063, doi:10.1046/j.1365-3091.1999.00264.x.

Etling, D., F. Gelhardt, U. Schrader, F. Brennecke, G. Kühn, G. Chabert D'Hieres, and H. Didelle (2000), Experiments with density currents on a sloping bottom in a rotating fluid, *Dyn. Atmos. Oceans*, *31*, 139–164, doi:10.1016/S0377-0265(99)00031-7.

Fer, I., G. Voet, K. S. Seim, B. Rudels, and K. Latarius (2010), Intense mixing of the Faroe Bank Channel overflow, *Geophys. Res. Lett.*, *37*, L02604, doi:10.1029/2009GL041924.

Flood, R. D., R. N. Hiscott, and A. E. Aksu (2009), Morphology and evolution of an anastomosed channel network where saline underflow enters the Black Sea, *Sedimentology*, *56*, 807–839, doi:10.1111/j.1365-3091.2008.00998.x.

Fugate, D. C., C. T. Friedrichs, and L. P. Sanford (2007), Lateral dynamics and associated transport of sediment in the upper reaches of a partially mixed estuary, Chesapeake Bay, USA, *Cont. Shelf Res.*, *27*, 679–698, doi:10.1016/j.csr.2006.11.012.

Garcia, M. H., and G. Parker (1993), Experiments on the entrainment of sediment into suspension by a dense bottom current, *J. Geophys. Res.*, *98*, 4793–4807, doi:10.1029/92JC02404.

Gray, T. E., J. Alexander, and M. R. Leeder (2006), Longitudinal flow evolution and turbulence structure of dynamically similar, sustained, saline density and turbidity currents, *J. Geophys. Res.*, *111*, C08015, doi:10.1029/2005JC003089.

Griffiths, R. W. (1986), Gravity currents in rotating systems, *Annu. Rev. Fluid Mech.*, *18*, 59–89, doi:10.1146/annurev.fl.18.010186.000423.

Hallworth, M. A., H. E. Huppert, and M. Ungarish (2001), Axisymmetric gravity currents in a rotating system: Experimental and numerical investigations, *J. Fluid Mech.*, *447*, 1–29.

Hart, J. E. (1971), Instability and secondary motion in a rotating channel flow, *J. Fluid Mech.*, *45*, 341–351, doi:10.1017/S0022112071000077.

Hay, A. E. (1987), Turbidity currents and submarine channel formation in Rupert Inlet, British Columbia: 2. The roles of continuous and surge-type flow, *J. Geophys. Res.*, *92*, 2883–2900, doi:10.1029/JC092iC03p02883.

Hesse, R., S. K. Chough, and A. Rakofsky (1987), The Northwest Atlantic Mid-Ocean Channel of the Labrador Sea. V. Sedimentology of a giant deep-sea channel, *Can. J. Earth Sci.*, *24*, 1595–1624.

Hiscott, R. N., F. R. Hall, and C. Pirmez (1997), Turbidity-current overspill from the Amazon channel: Texture of the silt/sand load, paleoflow from anisotropy of magnetic susceptibility and implications for flow processes, *Proc. Ocean Drill. Program Sci. Results*, *155*, 53–78.

Huppert, H. E. (1998), Quantitative modelling of granular suspension flows, *Philos. Trans. R. Soc. London, Ser. A*, *356*(1747), 2471–2496.

Imran, J., G. Parker, and C. Pirmez (1999), A nonlinear model of flow in meandering submarine and subaerial channels, *J. Fluid Mech.*, *400*, 295–331, doi:10.1017/S0022112099006515.

Imran, J., M. Islam, H. Huang, A. Kassem, C. Pirmez, J. Dickerson, and G. Parker (2007), Helical flow couplets in submarine gravity underflows, *Geology*, *35*, 659–662, doi:10.1130/G23780A.1.

Islam, M. A., and J. Imran (2008), Experimental modeling of gravity underflow in a sinuous submerged channel, *J. Geophys. Res.*, *113*, C07041, doi:10.1029/2007JC004292.

Islam, M. A., J. Imran, C. Pirmez, and A. Cantelli (2008), Flow splitting modifies the helical motion in submarine channels, *Geophys. Res. Lett.*, *35*, L22603, doi:10.1029/2008GL034995.

Ivanov, V. V., G. I. Shapiro, J. M. Huthnance, D. L. Aleynik, and P. N. Golovin (2004), Cascades of dense water around the world ocean, *Prog. Oceanogr.*, *60*, 47–98, doi:10.1016/j.pocean.2003.12.002.

Johnson, C. C., and D. R. Ohlsen (1994), Frictionally modified rotating hydraulic channel exchange and ocean outflows, *J. Phys. Oceanogr.*, *24*, 66–78, doi:10.1175/1520-0485(1994)024<0066:FMRHCE>2.0.CO;2.

Johnson, D. A., S. E. McDowell, L. G. Sullivan, and P. E. Biscaye (1976), Abyssal hydrography, nephelometry, currents, and benthic boundary layer structure in the Vema Channel, *J. Geophys. Res.*, *81*, 5771–5786, doi:10.1029/JC081i033p05771.

Johnson, G. C., and T. B. Sanford (1992), Secondary circulation in the Faroe bank channel outflow, *J. Phys. Oceanogr.*, *22*, 927–933, doi:10.1175/1520-0485(1992)022<0927:SCITFB>2.0.CO;2.

Kampf, J., and H. Fohrmann (2000), Sediment-driven downslope flow in submarine canyons and channels: Three-dimensional numerical experiments, *J. Phys. Oceanogr.*, *30*, 2302–2319, doi:10.1175/1520-0485(2000)030<2302:SDDFIS>2.0.CO;2.

Keevil, G. M., J. Peakall, J. L. Best, and K. J. Amos (2006), Flow structure in sinuous submarine channels: Velocity and turbulence structure of an experimental submarine channel, *Mar. Geol.*, *229*, 241–257, doi:10.1016/j.margeo.2006.03.010.

Khripounoff, A., A. Vangriesheim, N. Babonneau, P. Crassous, B. Dennielou, and B. Savoye (2003), Direct observation of intense turbidity current activity in the Zaire submarine valley at 4000 m water depth, *Mar. Geol.*, *194*, 151–158, doi:10.1016/S0025-3227(02)00677-1.

Klaucke, I., R. Hesse, and W. B. F. Ryan (1997), Flow parameters of turbidity currents in a low-sinuosity giant deep-sea channel, *Sedimentology*, *44*, 1093–1102.

Klaucke, I., R. Hesse, and W. B. F. Ryan (1998), Seismic stratigraphy of the Northwest Atlantic Mid-Ocean Channel: Growth pattern of a mid-ocean channel-levee complex, *Mar. Pet. Geol.*, *15*, 575–585, doi:10.1016/S0264-8172(98)00044-0.

Kneller, B. C., and C. Buckee (2000), The structure and fluid mechanics of turbidity currents: A review of some recent studies and their geological implications, *Sedimentology*, *47*, 62–94, doi:10.1046/j.1365-3091.2000.047s1062.x.

Kneller, B. C., S. J. Bennett, and W. D. McCaffrey (1999), Velocity structure, turbulence and fluid stresses in experimental gravity currents, *J. Geophys. Res.*, *104*, 5381–5391, doi:10.1029/1998JC900077.

Komar, P. D. (1969), The channelized flow of turbidity currents with application to Monterey deep-sea fan channel, *J. Geophys. Res.*, *74*, 4544–4558, doi:10.1029/JC074i018p04544.

Meiburg, E., and B. C. Kneller (2010), Turbidity currents and their deposits, *Annu. Rev. Fluid Mech.*, *42*, 135–156, doi:10.1146/annurev-fluid-121108-145618.

Menard, H. W. (1955), Deep-sea channels, topography, and sedimentation, *Am. Assoc. Pet. Geol. Bull.*, *39*, 236–255.

Middleton, G. V. (1993), Sediment deposition from turbidity currents, *Annu. Rev. Earth Planet. Sci.*, *21*, 89–114, doi:10.1146/annurev.ea.21.050193.000513.

Nidzieko, N. J., J. L. Hench, and S. G. Monismith (2009), Lateral circulation in well-mixed and stratified estuarine flows with curvature, *J. Phys. Oceanogr.*, *39*, 831–851, doi:10.1175/2008JPO4017.1.

Nof, D. (1996), Rotational turbidity flows and the 1929 grand banks earthquake, *Deep Sea Res., Part I*, *43*, 1143–1163, doi:10.1016/0967-0637(96)00041-6.

Normark, W. R. (1989), Observed parameters for turbidity-current flow in channels, Reserve Fan, Lake Superior, *J. Sediment. Petrol.*, *59*, 423–431.

Normark, W. R., and F. H. Dickson (1976), Man-made turbidity currents in Lake Superior, *Sedimentology*, *23*, 815–831, doi:10.1111/j.1365-3091.1976.tb00110.x.

Ott, M. W., R. Dewey, and C. Garrett (2002), Reynolds stresses and secondary circulation in a stratified rotating shear flow, *J. Phys. Oceanogr.*, *32*, 3249–3268, doi:10.1175/1520-0485(2002)032<3249:RSASCI>2.0.CO;2.

Özsoy, E., D. Di Iorio, M. Gregg, and J. O. Backhaus (2001), Mixing in the Bosphorus Strait and the Black Sea continental shelf: Observations and a model of the dense water outflow, *J. Mar. Syst.*, *31*, 99–135, doi:10.1016/S0924-7963(01)00049-5.

Peakall, J., B. McCaffrey, and B. C. Kneller (2000), A process model for the evolution, morphology and architecture of sinuous submarine channels, *J. Sediment. Res.*, *70*, 434–448, doi:10.1306/2DC4091C-0E47-11D7-8643000102C1865D.

Peakall, J., K. J. Amos, G. M. Keevil, P. W. Bradbury, and S. Gupta (2007), Flow processes and sedimentation in submarine channel bends, *Mar. Pet. Geol.*, *24*, 470–486, doi:10.1016/j.marpetgeo.2007.01.008.

Pirmez, C., and J. Imran (2003), Reconstruction of turbidity currents in Amazon Channel, *Mar. Pet. Geol.*, *20*, 823–849, doi:10.1016/j.marpetgeo.2003.03.005.

Price, J. F., and M. O. Baringer (1994), Outflows and deep water production by marginal seas, *Prog. Oceanogr.*, *33*, 161–200, doi:10.1016/0079-6611(94)90027-2.

Rhoads, B. L., and M. R. Welford (1991), Initiation of river meandering, *Prog. Phys. Geogr.*, *15*, 127–156, doi:10.1177/030913339101500201.

Sherwin, T. (2010), Observations of the velocity profile of a fast and deep oceanic density current constrained in a gully, *J. Geophys. Res.*, *115*, C03013, doi:10.1029/2009JC005557.

Shipboard Scientific Party (1995), Leg synthesis, *Proc. Ocean Drill. Program Initial Rep.*, *155*, 17–21.

Straub, K. M., D. Mohrig, B. McElroy, J. Buttles, and C. Pirmez (2008), Interactions between turbidity currents and topography in aggrading sinuous submarine channels: A laboratory study, *Geol. Soc. Am. Bull.*, *120*, 368–385, doi:10.1130/B25983.1.

Umlauf, L., and L. Arneborg (2009a), Dynamics of rotating shallow gravity currents passing through a channel. Part I: Observation of transverse structure, *J. Phys. Oceanogr.*, *39*, 2385–2401, doi:10.1175/2009JPO4159.1.

Umlauf, L., and L. Arneborg (2009b), Dynamics of rotating shallow gravity currents passing through a channel. Part II: Analysis, *J. Phys. Oceanogr.*, *39*, 2402–2416, doi:10.1175/2009JPO4164.1.

Ungarish, M., and H. E. Huppert (1999), Simple models of Coriolis-influenced axisymmetric particle-driven gravity currents, *Int. J. Multiphase Flow*, *25*, 715–737, doi:10.1016/S0301-9322(98)00062-7.

Voulgaris, G., and J. H. Trowbridge (1998), Evaluation of the acoustic Doppler velocimeter (ADV) for turbulence measurements, *J. Atmos. Oceanic Technol.*, *15*, 272–289, doi:10.1175/1520-0426(1998)015<0272:EOTADV>2.0.CO;2.

Wåhlin, A. K. (2002), Topographic steering of dense currents with application to submarine canyons, *Deep Sea Res., Part I*, *49*, 305–320, doi:10.1016/S0967-0637(01)00058-9.

Wåhlin, A. K. (2004), Downward channeling of dense water in topographic corrugations, *Deep Sea Res., Part I*, *51*, 577–590, doi:10.1016/j.dsr.2003.11.002.

Wåhlin, A. K., E. Darelius, C. Cenedese, and G. F. Lane-Serff (2008), Laboratory observations of enhanced entrainment in dense overflows in the presence of submarine canyons and ridges, *Deep Sea Res., Part I*, *55*, 737–750, doi:10.1016/j.dsr.2008.02.007.

Weatherly, G. L., and P. J. Martin (1978), On the structure and dynamics of the oceanic bottom boundary layer, *J. Phys. Oceanogr. 8*, 557–570, doi:10.1175/1520-0485(1978)008<0557:OTSADO>2.0.CO;2.

Weimer, P., R. M. Slatt, P. Dromgoole, M. Bowman, and A. Leonard (2000), Developing and managing turbidite reservoirs: Case histories and experiences: Results of the 1998 EAGE/AAPG Research Conference, *AAPG Bull.*, *84*, 453–465.

Wells, M. G. (2009), How Coriolis forces can limit the spatial extent of sediment deposition of a large-scale turbidity current, *Sediment. Geol.*, *218*, 1–5, doi:10.1016/j.sedgeo.2009.04.011.

Wells, M. G., and P. Nadarajah (2009), The intrusion depth of density currents flowing into stratified water bodies, *J. Phys. Oceanogr.*, *39*, 1935–1947, doi:10.1175/2009JPO4022.1.

Wells, M. G., and J. S. Wettlaufer (2007), The long-term circulation driven by density currents in a two-layer stratified basin, *J. Fluid Mech.*, *572*, 37–58, doi:10.1017/S0022112006003478.

Wells, M. G., C. Cenedese, and C. P. Caulfield (2010), The relationship between flux coefficient and entrainment ratio in density currents, *J. Phys. Oceanogr.*, doi:10.1175/2010JPO4225.1, in press.

Wood, L. J., and K. L. Mize-Spansky (2009), Quantitative seismic geomorphology of a Quaternary leveed-channel system, offshore eastern Trinidad and Tobago, northeastern South America, *AAPG Bull.*, *93*, 101–125, doi:10.1306/08140807094.

Xu, J. P., M. A. Noble, and L. K. Rosenfeld (2004), In-situ measurements of velocity structure within turbidity currents, *Geophys. Res. Lett.*, *31*, L09311, doi:10.1029/2004GL019718.

R. Cossu, Department of Geology, University of Toronto, 22 Russell St., Toronto, ON M5S 3B1, Canada. (remo.cossu@utoronto.ca)

A. K. Wåhlin, Department of Earth Sciences, University of Gothenburg, PO Box 460, SE-405 30 Göteborg, Sweden. (awahlin@gu.se)

M. G. Wells, Department of Physical and Environmental Sciences, University of Toronto, 1265 Military Trail, Toronto, ON M1C 1A4, Canada. (wells@utsc.utoronto.ca)